

Robust parameter estimation within minutes on gravitational wave signals from binary neutron star inspirals

Thibeau Wouters ^{1, 2,*} Peter T. H. Pang Tim Dietrich ^{3, 4} and Chris Van Den Broeck ^{1, 2}

¹*Institute for Gravitational and Subatomic Physics (GRASP),
Utrecht University, Princetonplein 1, 3584 CC Utrecht, The Netherlands*

²*Nikhef, Science Park 105, 1098 XG Amsterdam, The Netherlands*

³*Institut für Physik und Astronomie, Universität Potsdam,
Haus 28, Karl-Liebknecht-Str. 24/25, 14476, Potsdam, Germany*

⁴*Max Planck Institute for Gravitational Physics (Albert Einstein Institute), Am Mühlenberg 1, Potsdam 14476, Germany*

(Dated: April 18, 2024)

The gravitational waves emitted by binary neutron star inspirals contain information on nuclear matter above saturation density. However, extracting this information and conducting parameter estimation remains a computationally challenging and expensive task. Wong et al. introduced JIM [1], a parameter estimation pipeline that combines relative binning and JAX features such as hardware acceleration and automatic differentiation into a normalizing flow-enhanced sampler for gravitational waves from binary black hole (BBH) mergers. In this work, we extend the JIM framework to analyze gravitational wave signals from binary neutron star (BNS) mergers with tidal effects included. We demonstrate that JIM can be used for full Bayesian parameter estimation of gravitational waves from BNS mergers within a few tens of minutes, which includes the training of the normalizing flow and computing the reference parameters for relative binning. For instance, JIM can analyze GW170817 in 26 minutes (33 minutes) of total wall time using the `TaylorF2` (`IMRPhenomD_NRTidalv2`) waveform, and GW190425 in around 21 minutes for both waveforms. We highlight the importance of such an efficient parameter estimation pipeline for several science cases as well as its ecologically friendly implementation of gravitational wave parameter estimation.

I. INTRODUCTION

Neutron stars (NSs) are the remnants of core-collapse supernovae and consist of the densest matter ever observed in the Universe [2, 3]. With densities up to a few times the nuclear saturation density $n_{\text{sat}} = 2.7 \times 10^{14} \text{ g cm}^{-3}$, NSs are the perfect laboratories for studying the properties and behavior of ultra-dense matter. The equation of state (EOS) relates the pressure, temperature, and energy density within the interior of NSs and is not completely understood [4]. It is defined by the fundamental degrees of freedom within the NS and the interactions among them. Each proposed EOS uniquely dictates the global structure of NSs, influencing their masses, radii, and tidal deformabilities [5–7]. Thus, astronomical observations of NSs allow one to constrain the EOS in NSs [8–18].

Since the first detection of gravitational waves (GWs) from a BNS merger in 2017 [19], by Advanced LIGO [20] and Advanced Virgo [21], GW astronomy has become an important channel for astronomical observation of NSs. An essential step for extracting physics from the GW data is performing parameter estimation (PE) on it.

Within the community, multiple central processing unit (CPU)-based PE software packages have been developed, which include LALINFERENC [22], PYCBC INFERENC [23] and BILBY [24–26]. These packages are robust and have been used for analyzing multiple GW

events [19, 27]. Yet, they are also known for being computationally expensive and having a large carbon footprint, especially for analyzing BNS events. For these reasons, a lot of effort has been put into developing methods to speed up PE, e.g., relative binning [28, 29] and reduced order quadrature (ROQ) [30, 31], which show substantial improvements [32, 33].

In addition, there have been proposals to accelerate PE through the use of graphical processing unit (GPU)-based software or machine learning (ML) techniques. One such technique, known as normalizing flows, has been gaining popularity in the field. For instance, DINGO uses normalizing flows pretrained on simulated data to approximate the posterior distribution [34–36]. Similarly, normalizing flows have been used to accelerate nested sampling for GW data analysis by NESSAI [37, 38]. Recently, a GPU-based PE software, JIM [1], has been introduced, which accelerates PE with Markov chain Monte Carlo (MCMC) samplers using normalizing flows. In Ref. [1], the authors demonstrated that JIM can conduct PE on GW signals within minutes of total wall time on a single GPU.

In this paper, we extend the capabilities of JIM to analyze GWs from BNS mergers, in particular to also infer the tidal deformabilities of GW signals. The updated JIM framework is crucial for low-latency PE, necessary for efficient telescopes' responses on BNS detections, for handling the PE for a large number of BNS events, and to aid the multi-messenger analysis on BNS via integration with a nuclear physics multi-messenger framework, e.g., NMMA [39]. As we show in more detail below, JIM performs these efficient runs at a lower carbon footprint

* t.r.i.wouters@uu.nl

compared to other existing pipelines.

This paper is structured as follows. In Sec. II, we give an overview of JIM and our methods, with their validation shown in Sec. III. In Sec. IV, we apply our methods on the two BNS GW detections to date, namely GW170817 [19] and GW190425 [27]. We compare our work to other methods and discuss implications for future work in Sec. V. Concluding remarks and future perspectives are provided in Sec. VI.

II. METHODS

A. Parameter estimation

Based on Bayes' theorem, the posterior distribution of the source parameters $\boldsymbol{\theta}$ of a GW signal d , denoted by $p(\boldsymbol{\theta}|d)$, is given by [40]

$$p(\boldsymbol{\theta}|d) = \frac{p(d|\boldsymbol{\theta})p(\boldsymbol{\theta})}{p(d)}, \quad (1)$$

where $p(d|\boldsymbol{\theta})$ is the likelihood function, $p(\boldsymbol{\theta})$ is the prior probability distribution and $p(d)$ is the Bayesian evidence. Under the assumption of stationary Gaussian noise, the log-likelihood function for the waveform $h(\boldsymbol{\theta})$ is given by

$$\log p(d|\boldsymbol{\theta}) = -\frac{1}{2} \langle d - h(\boldsymbol{\theta}), d - h(\boldsymbol{\theta}) \rangle + \text{constant}, \quad (2)$$

where the inner product $\langle a, b \rangle$ is defined as

$$\langle a, b \rangle = 4\Re \int_{f_{\text{low}}}^{f_{\text{high}}} df \frac{\tilde{a}(f)\tilde{b}^*(f)}{S_n(f)}, \quad (3)$$

with $S_n(f)$ being the one-sided power spectral density (PSD), $\tilde{x}(f)$ being the Fourier transform of $x(t)$, and the asterisk denoting the complex conjugate. In this work, the frequency range of the integral is chosen such that it covers the frequency span of the signal, which for BNS signals is usually taken as [20, 2048] Hz. A complete list of parameters and corresponding definitions can be found in Ref. [25]. The notation used in this work can be found in Tab. II.

B. Waveform approximants

Several families of waveform approximants have been developed and are used in GW data analysis. These families are mainly divided into the post-Newtonian (PN) waveforms [41, 42], the effective one-body waveforms [43–45], such as TEOBResumS [46–48] or SEOBNRv4T [49, 50] for BNS inspirals, the inspiral-merger-ringdown phenomenological (IMRPhenom) waveforms, such as IMRPhenomD for BBH inspirals [51, 52], or surrogate models based on numerical-relativity simulations [53]. In this

work, we will limit ourselves to the frequency domain approximants TaylorF2, which is a PN approximant, and IMRPhenomD_NRTidalv2 [54, 55], which are both frequently used in the analysis of BNS events. We do not consider the recently introduced IMRPhenomXAS_NRTidalv2 [56] or NRTidalv3 models [57], since these waveform models are not released at the time of writing.

C. Relative binning

Relative binning [29, 32, 58] is a technique to speed up the evaluation of the likelihood function given in Eq. (2). Given a reference parameter $\boldsymbol{\theta}_{\text{ref}}$, the ratio $r(f)$ of the waveform of an arbitrary parameter $\boldsymbol{\theta}$ against the reference waveform is given by

$$r(f) = \frac{h(f; \boldsymbol{\theta})}{h(f; \boldsymbol{\theta}_{\text{ref}})} = \left| \frac{A(f)}{A_{\text{ref}}(f)} \right| e^{-i(\Psi(f) - \Psi_{\text{ref}}(f))}. \quad (4)$$

The above ratio can be approximated by piecewise linear functions, i.e.,

$$r(f) \approx \begin{cases} r_0(b_1) + r_1(b_1)(f - f_m(b_1)), & f \in b_1 \\ r_0(b_2) + r_1(b_2)(f - f_m(b_2)), & f \in b_2 \\ \vdots \\ r_0(b_n) + r_1(b_n)(f - f_m(b_n)). & f \in b_n \end{cases} \quad (5)$$

Thus, the ratio is approximated with frequencies split into bins $\{b_i\}$, with central frequencies $\{f_m(b_i)\}$. Such an approximation can reach an arbitrary accuracy provided that a sufficiently high number of bins b_i is used. However, to speed up the PE, one would aim for approximating the above ratio with the least number of bins. The relative binning method assumes that the region of parameter space with a non-negligible likelihood overlaps with the region for which the waveforms only differ from the best-fit waveform by small perturbations. Thus the ratio $r(f)$ is a smooth function that can be well approximated with a low number of bins.

The bin placement often follows the approach described in Ref. [29]. In this scheme, one assumes that the variations in the ratio of amplitudes can be neglected. The error on the ratio is therefore determined by the deviations in the phase, and one can place the bin edges in such a way to ensure that the deviation in the phase across a bin is below a certain desired threshold. This deviation is approximated with an ansatz of the phase based on PN theory to remove the dependence on the waveform's parameters. We refer readers to Refs. [29, 32] for further details.

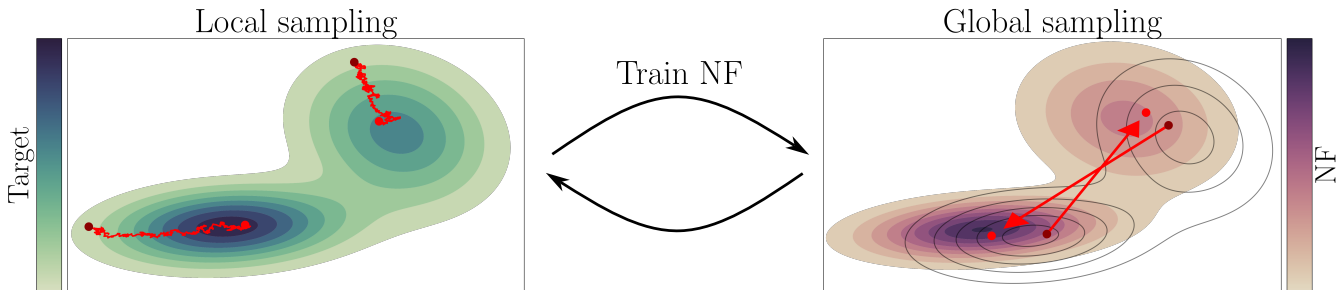


FIG. 1: Schematic overview of the training loop of the FLOWMC sampler. Each loop starts with running the local sampler. For the local sampling, we use the Metropolis-adjusted Langevin algorithm (MALA) algorithm, which exploits the gradient of the target distribution (green and gray lines) to evolve the Markov chains (red). With the samples obtained from the local sampler, a normalizing flow (NF) is trained to approximate the distribution of the Markov chains. During the global sampling phase, we use the density learned by the NF (purple) as a proposal. We accept or reject the proposed samples (red) with a Metropolis-Hastings step, which relies on both the proposal density as well as the target density. This local-global procedure is repeated until the NF has converged. Afterward, we perform a fixed number of production loops, where the weights of the NF are frozen and the local and global sampler output the final production samples.

1. Caveats for applying relative binning with NRTidal-family waveforms

The above assumption regarding the amplitude ratio holds for a majority of waveform models (e.g., TaylorF2). However, it is invalid for the `IMRPhenomD_NRTidalv2` waveform model. This waveform model modifies its underlying point-particle baseline, `IMRPhenomD`, with closed-form expressions for the tidal contributions to the phase and amplitude. These are modeled by Padé approximants, such that the PN ansatz for the phase used in placing the bin edges is no longer a valid approximation. Moreover, `IMRPhenomD_NRTidalv2` additionally tapers the waveform so that its amplitude transitions smoothly to zero in the range $[f_{\text{merger}}, 1.2f_{\text{merger}}]$, where the merger frequency f_{merger} depends on the intrinsic source parameters and was estimated through a phenomenological relation [55]. For larger deviations from the reference parameters, this causes the ratio of amplitudes in Eq. (4) to vary significantly, causing a breakdown of the relative binning scheme. Moreover, we observed that, for some parameter regimes for which the reference waveform has a low merger frequency, the ratio of amplitudes becomes numerically unstable. Therefore, we generate the reference waveform without the tapering window when analyzing simulated signals in Sec.III below.

2. Reference parameters

Relative binning requires a set of reference parameters as input that, ideally, lie close to the best-fit parameters. When analyzing simulated signals, we set the reference parameters equal to the injected parameters. For analyzing real events, we first perform a heuristic search to

obtain an estimate of the maximum likelihood parameters. More specifically, we employ the covariance matrix adaptation evolution strategy (CMA-ES) [59] as implemented in EVOSAX [60] before running JIM to obtain the reference parameters used in the PE run.

D. Jim

JIM [1] is a PE pipeline to analyze GW events involving BBH mergers that is able to run on CPUs, GPUs or tensor processing units (TPUs). In Ref. [1], the authors demonstrated JIM’s capability of performing PE in the order of minutes of total wall-time, including training of the normalizing flow. In this work, we extend JIM’s capability of performing PE on GW signals from BNS inspirals with tidal effects included.

JIM is implemented in JAX [61], a high-performance numerical computation library. JAX has a number of desirable features for GW data analysis, such as i) automatic differentiation, allowing the use of gradient-based MCMC samplers, ii) native support for hardware accelerators, such as GPUs or TPUs, and iii) just-in-time (JIT) compilation to further accelerate the execution of the code.

For our waveform generator, we make use of the RIPPLE [62], a JAX package for differentiable waveform approximants. To analyze BNS signals, we extend RIPPLE with the TaylorF2 and `IMRPhenomD_NRTidalv2` waveform models.^{1,2}

¹While TaylorF2 and `IMRPhenomD_NRTidalv2` already have an existing JAX implementation in GWFAST [63], we choose to provide an independent implementation in RIPPLE in order to interface more easily with JIM and FLOWMC.

²We note that Ref. [64] has used TaylorF2 with JIM for PE. How-

For the MCMC sampler, we employ FLOWMC, a JAX-based MCMC sampler that makes use of gradient-based samplers and is enhanced by normalizing flows [65, 66]. The principle behind the FLOWMC sampler is summarized by the diagram in Fig. 1. FLOWMC combines a local and global proposal distribution to improve the sampler’s efficiency. For the local sampler, we use the Metropolis-adjusted Langevin algorithm (MALA) routine [67], which exploits the gradient of the posterior distribution to evolve the Markov chains. The global sampler is parameterized by a normalizing flow (NF), which is implemented with EQUINOX [68]. NFs are deep generative models that offer tractable approximations of complex probability distributions, allowing for efficient and precise sampling as well as density evaluation. In FLOWMC, the NF is trained from the samples generated by the local sampler and subsequently used as proposal distribution for the global sampling phase.

The sampler settings can be either optimized for speed or accuracy. In this work, we use settings that focus on the latter. For instance, to improve the robustness of the sampler, we use a stopping threshold. Once the NF achieves a preset threshold value for the mean acceptance rate during the Metropolis-Hastings steps, the NF is frozen, and the final production samples are produced by only running the local and global samplers (known as the production loop) for a fixed amount of epochs. Training of the NF dominates the wall time, while the production loop only takes 1-2 minutes.

III. VALIDATION

In this section, we validate our methods before applying them to real GW data in Sec. IV. In particular, we check the accuracy of the waveforms implemented in RIPPLE and verify the robustness of our pipeline via an injection-recovery test.

A. Accuracy of RIPPLE waveforms

We verify the correctness of our waveform generators by comparing them against the LALSUITE [69] implementation. This is done by computing the mismatch M between the waveforms generated by the two implementations, which is defined by

$$M(h_1, h_2) \equiv 1 - \max_{\Delta t_c, \Delta \phi_c} \frac{\langle h_1, h_2 \rangle}{\sqrt{\langle h_1, h_1 \rangle \langle h_2, h_2 \rangle}}, \quad (6)$$

where Δt_c and $\Delta \phi_c$ represent the difference between the time of coalescence and the phase of coalescence of the two waveforms, respectively.

ever, here we provide an extensive validation of the implementation and provide detailed benchmarks.

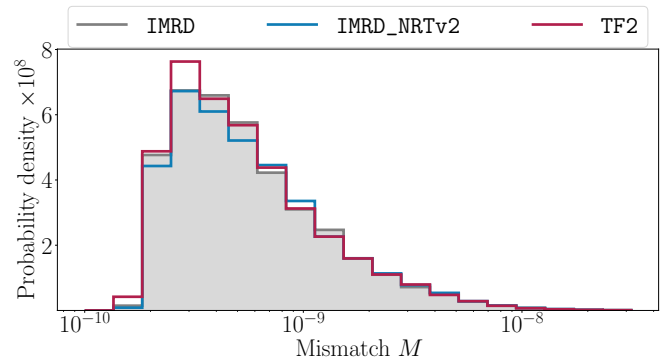


FIG. 2: Distribution of mismatch values between RIPPLE and LALSUITE implementations of the `IMRPhenomD` (IMRD), `IMRPhenomD_NRTidalv2` (IMRD_NRTv2) and `TaylorF2` (TF2) waveforms. For both newly added waveform models, the probability mass peaks at a mismatch below 10^{-8} , indicating consistency with the LALSUITE implementation.

| Parameter | Range |
|-------------------------------------|--------------------------|
| Component masses | $[0.5M_\odot, 3M_\odot]$ |
| Component aligned spins | $[-0.05, 0.05]$ |
| Dimensionless tidal deformabilities | $[0, 5000]$ |
| Inclination angle | $[0, \pi]$ |

TABLE I: Parameter ranges for the mismatch calculation. All parameters are distributed uniformly in the specified ranges.

In Fig. 2, the distribution of the mismatch between the RIPPLE waveforms against the corresponding LALSUITE implementation is shown. Specifically, we have sampled 10000 parameters from the distributions shown in Tab. I. The mismatch is computed on a frequency grid in the range [20, 2048] Hz with spacing $\Delta f = 1/T$, where we take the duration T to be 128 s, and with the design sensitivity of Advanced LIGO [20] used for the PSD. For comparison, we also show the mismatches for RIPPLE’s BBH waveform `IMRPhenomD` for the same parameter ranges, excluding the tidal deformabilities. All RIPPLE waveform samples have mismatches $M \lesssim 10^{-8}$ against their LALSUITE counterpart, making them indistinguishable for parameter estimation [70].

B. Injection-recovery test

To demonstrate the robustness of our PE pipeline, we perform injection-recovery tests and report the results in a percentile-percentile (p-p) plot [71]. We inject simulated GW signals into realizations of noise from a detector network and conduct PE on the simulated data with JIM. After performing a batch of such analyses, we calculated the credible level at which each true parameter appears in its marginal posterior distribution. If the

pipeline delivers unbiased estimates of the source properties, it is expected that the true parameters occur in the $x\%$ credible interval $x\%$ of the time. Therefore, the cumulative distribution of the credible level should trend along the diagonal, which is often checked visually with a p-p plot.

For both waveforms considered here, we create 100 GW events by sampling source parameters uniformly over the ranges given in Tab. II. We reject sampled injection parameters that result in a signal-to-noise ratio below 12. The duration is set to 128 s, with a frequency range of [20, 2048] Hz. The synthetic GW signal is injected into a network consisting of the Advanced LIGO [20] and Advanced Virgo [21] detectors at their design sensitivities. We evolve 1000 Markov chains and stop the FLOWMC training phase once the NF achieves an average acceptance rate of 20%. Instead of the individual aligned spins, we show the effective spin χ_{eff} , defined by

$$\chi_{\text{eff}} = \frac{m_1 \chi_1 + m_2 \chi_2}{m_1 + m_2}. \quad (7)$$

The resulting p-p plots are shown in Fig. 3. Since the plots generally trend along the diagonal, we conclude that our pipeline is robust.

IV. ANALYSIS ON GW170817 AND GW190425

With the robustness of our pipeline demonstrated, we apply JIM to the two BNS events observed so far: GW170817 [19] and GW190425 [27].³ For both events, we take the publicly available data from GWOSC [77, 78] as input. The priors used in the analysis are reported in Tab. II.

For comparison, we have conducted the PE with both TaylorF2 and IMRPhenomD_NRTidalv2 using both JIM and PARALLEL-BILBY (PBILBY) [26] to verify the accuracy of JIM. As mentioned in Sec. II C, JIM utilizes relative binning, employing EVOSAX to search for the reference parameters. We 1000 Markov chains and stop the FLOWMC training phase once the NF achieves an average acceptance rate of 10%. The resulting posterior samples are compared in Sec. IV A, and the run times are compared in Sec. IV B.

A. Posterior comparison

In Figures 4 to 7 in Appendix B, we show the visual comparison between the posterior samples obtained from JIM and PBILBY and find agreement between the posteriors. To make a quantitative statement, we report

the Jensen-Shannon (JS) divergences [79] in bits between the marginal distributions in Tab. III. Since the JS divergences lie between 0 and 1 and the highest JS divergence is 0.01847 bits (0.014136 bits) for GW170817 (GW190425), we conclude that the results of the JIM and PBILBY pipelines are consistent with each other.

B. Wall time

We report the total wall time spent on the PE for the real and simulated events mentioned in this work in Tab. IV. We run JIM on a single NVIDIA A100-40 GB GPU.

Each wall time of JIM mentioned below includes the time spent on the JIT compilation of the code and calculating the summary data used in relative binning, which on average takes around 2.5 minutes.

For the analysis of the real events, the wall time of JIM additionally includes the time spent on calculating the reference parameters with EVOSAX to initialize the relative binning likelihood, which takes between 5 and 10 minutes. Most of the wall time is spent on the training of the NF, which takes around 15 minutes for the real events, after which the final production samples are produced in less than a minute. We remark that the sampling time for GW170817 with the IMRPhenomD_NRTidalv2 waveform is slightly higher, since 10 times more bins were used in the relative binning method to achieve a reliable approximation, due to the breakdown of relative binning as discussed in Sec. II C 1.

For the injected events, we report the median value for the runtime of the PE runs performed with both waveforms. Since we set the reference parameters to the injected parameters, the runtime no longer includes any runtime from running the EVOSAX algorithm. We note that the wall time for simulated events is slightly higher than that of real events. This is because we have adjusted the sampling settings to be more robust to accommodate the broadly distributed simulated events in terms of signal-to-noise ratio and chirp masses. While the evaluation of the IMRPhenomD_NRTidalv2 waveform is slower than the TaylorF2 waveform, we note that the speed of JIM is mainly determined by the convergence rate of the NF, the value for the stopping criterion chosen by the user and the number of bins used in relative binning.

We note that Ref. [1] achieved wall times of a few minutes for analyzing BBH mergers with JIM. In our case, the wall time is higher, partly due to the increased dimensionality of the problem by including the tidal deformabilities, but mainly because of different sampler settings. In particular, our settings aim for robustness rather than speed by training the NF until it achieves an average acceptance rate of 10% (20%) for the real events (injections). On the other hand, the settings chosen in Ref. [1] resulted in an average acceptance rate of 2% – 5% for the NF.

Finally, for the real events, the wall times are com-

³While GW170817 has been confidently verified to be a BNS merger, there have been proposals that GW190425 could be a neutron-star–black-hole merger [72–76].

| Parameter | Description | Injection | GW170817 | GW190425 |
|---------------|---|---------------|---------------|----------------|
| \mathcal{M} | detector-frame chirp mass [M_\odot] | [0.88, 2.61] | [1.18, 1.21] | [1.485, 1.490] |
| q | mass ratio | [0.5, 1] | [0.125, 1] | [0.125, 1] |
| χ_i | aligned spins | [-0.05, 0.05] | [-0.05, 0.05] | [-0.05, 0.05] |
| Λ_i | dimensionless tidal deformabilities | [0, 5000] | [0, 5000] | [0, 5000] |
| d_L | luminosity distance [Mpc] | [30, 300] | [1, 75] | [1, 500] |
| t_c | coalescence time [s] | [-0.1, 0.1] | [-0.1, 0.1] | [-0.1, 0.1] |
| ϕ_c | coalescence phase | [0, 2π] | [0, 2π] | [0, 2π] |
| $\cos \iota$ | cosine of inclination angle | [-1, 1] | [-1, 1] | [-1, 1] |
| ψ | polarization angle | [0, π] | [0, π] | [0, π] |
| α | right ascension | [0, 2π] | [0, 2π] | [0, 2π] |
| $\sin \delta$ | sine of declination | [-1, 1] | [-1, 1] | [-1, 1] |

TABLE II: Parameters used and their corresponding prior ranges for our analyses. All priors considered in this work are uniform priors with the specified range.

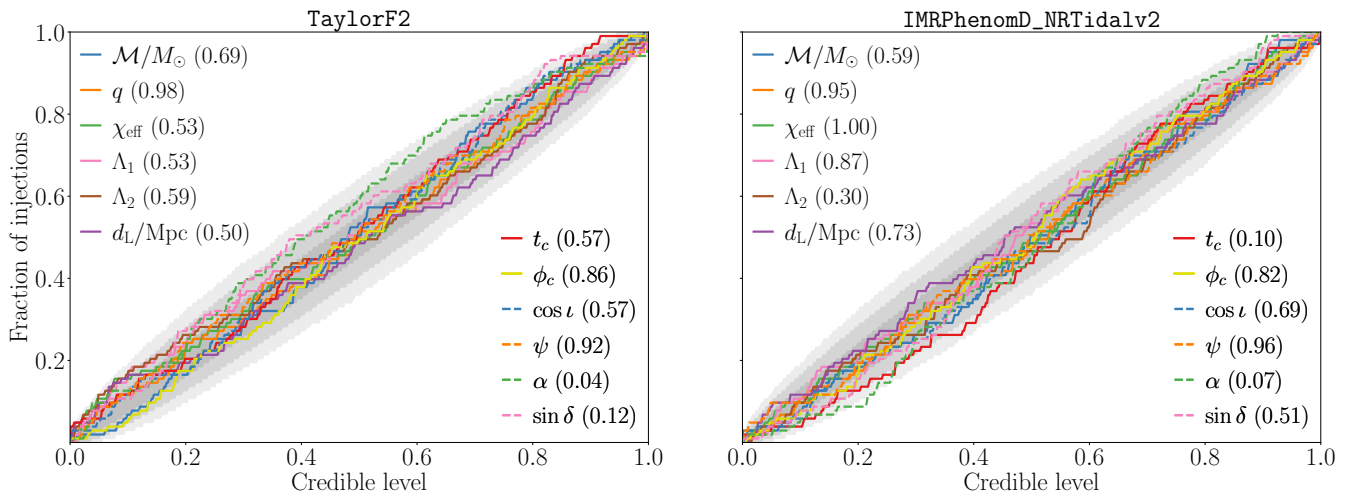


FIG. 3: p-p plot for the injections done with `TaylorF2` (left) and `IMRPhenomD_NRTidalv2` (right), each created from 100 injections. For both of the waveform models, the p-p plots agree well with the diagonal, demonstrating the robustness of the JIM pipeline on analyzing BNS signals. The shaded regions indicate the 1σ , 2σ and 3σ confidence levels due to finite sample sizes.

pared against their equivalent `PBILBY`, `BILBY` with relative binning (`RB-BILBY` [32]),⁴ and `BILBY` with ROQ (`ROQ-BILBY` [33]),⁵ in Tab. IV. ROQ is a technique that creates an efficient representation of GW approximants with a reduced set of basis elements that still accurately reconstruct the entire model space, thereby reducing the number of terms to be computed. These runs make use of nested sampling [80] with 1024, 1000 and 1000 live points for `PBILBY`, `RB-BILBY` and `ROQ-BILBY`, respectively. The `PBILBY` runs are intended to verify the accuracy of our pipeline. However, `PBILBY` is known to be expensive;

therefore, we use 10 Intel Skylake Xeon Platinum 8174 CPUs (480 cores in total) per run so that the PE completes in a reasonable amount of time. For `RB-BILBY` and `ROQ-BILBY`, we instead use a single Intel Xeon Silver 4310 Processor CPU, such that 24 cores are used per run.⁶

⁴The reference parameters are identical to the ones used by JIM.

⁵Due to the unavailability of the ROQ bases of `TaylorF2` with tidal effects and `IMRPhenomD_NRTidalv2`, the bases of `IMRPhenomPv2_NRTidalv2` is used.

⁶There are 12 physical cores on an Intel Xeon Silver 4310 Processor CPU. On the machines used, there are two such CPUs installed. When running with 24 cores requested, the CPUs dynamically switches between with and without hyper-threading [81]. For a conservative estimate of the energy consumption, we take only the thermal design power (TDP) of one CPU in Sec. V C.

| Parameter | GW170817 | | GW190425 | |
|---------------|-----------------|----------------|-----------------|-----------------|
| | TF2 | NRTv2 | TF2 | NRTv2 |
| \mathcal{M} | 0.001725 | 0.000516 | 0.003557 | 0.001884 |
| q | 0.005212 | 0.007894 | 0.004837 | 0.003883 |
| χ_1 | 0.005633 | 0.004301 | 0.002794 | 0.001904 |
| χ_2 | 0.003030 | 0.002671 | 0.002416 | 0.001400 |
| Λ_1 | 0.001062 | 0.002208 | 0.008556 | 0.000652 |
| Λ_2 | 0.000559 | 0.002186 | 0.005808 | 0.001450 |
| d_L | 0.001544 | 0.01847 | 0.001273 | 0.009157 |
| ϕ_c | 0.003500 | 0.010714 | 0.003338 | 0.007874 |
| $\cos \iota$ | 0.001615 | 0.012851 | 0.006400 | 0.009502 |
| ψ | 0.004048 | 0.011036 | 0.001516 | 0.005820 |
| α | 0.014008 | 0.001258 | 0.009822 | 0.014136 |
| $\sin \delta$ | 0.009570 | 0.001761 | 0.008934 | 0.006362 |

TABLE III: Jensen-Shannon divergences (in bits) between the marginal posterior obtained for GW170817 and GW190425 using TaylorF2 and IMRPhenomD_NRTidalv2 with JIM and PBILBY, with the highest value of each comparison in bold. The JS divergences are bound between [0, 1].

V. DISCUSSION

Our numerical experiments from the previous sections demonstrate that JIM can robustly analyze BNS mergers with high speed and without loss of accuracy. We discuss the implications of our pipeline for future work and compare our pipeline to other state-of-the-art pipelines that speed up PE.

A. Science cases

The robustness and speed-up offered by JIM are crucial to meet the computational requirements of challenging science studies. For instance, while sky maps can be produced in low latency with BAYESTAR [82], performing PE on the intrinsic parameters improves the knowledge of the source properties and would be essential to improve estimates of electromagnetic (EM) emission, such as the brightness of a potential kilonova; see, e.g., Ref. [83]. In general, good guidance for EM follow-up searches is critical for improving the scientific return of follow-up campaigns while on the other hand lowering the requirement for expensive telescope time. As such, the speed of JIM in performing PE offers a way to enhance low-latency follow-up strategies.

Furthermore, the next generation of GW detectors, such as Einstein Telescope [84], will have an overall greater sensitivity and broader frequency bandwidth compared to existing detectors [85–87]. Future detectors will observe more BNS inspirals, which will also be in the sensitive band for a longer time, calling for efficient and effective PE pipelines [88, 89].

B. Comparison to related works

Related works accelerating PE can be mainly divided into likelihood-based methods, which directly evaluate the likelihood, and likelihood-free methods, which bypass the likelihood evaluation and instead rely on surrogates of the likelihood or posterior. We note that JIM belongs to the former class of methods.

One likelihood-based method to speed up PE is relative binning and was discussed in Sec.II C. Previous works have used relative binning for multi-messenger and low-latency PE studies [90, 91]. Relative binning was also recently integrated into BILBY [32].

Another way to speed up the likelihood evaluation is through reduced order modelling (ROM) and ROQ methods. Using ROQ, previous works have been able to perform PE in the order of minutes [31, 33, 92]. However, ROQ requires precomputing these reduced bases, which can be computationally expensive, as we show with our estimate in Appendix C. While these bases have to be constructed only once, JIM, on the other hand, does not require any precomputed quantities as input for the PE.

Besides relative binning and ROQ, other approximations of the likelihood have been studied as well, such as approximating the likelihood with Gaussian processes [93–95], a mesh-free interpolation method [96, 97], or through marginalization of the likelihood, e.g. [98].

Apart from approximating the likelihood, ML can speed up sampling as well. For example, NESSAI accelerates nested sampling through normalizing flows [37]. Recently, this method achieved wall times similar to ours by combining NESSAI with the ROQ approximation [38]. While similar in spirit to our work, we note that JIM makes use of MCMC rather than nested sampling for exploring the likelihood landscape, and uses relative binning rather than ROQ to speed up likelihood evaluation, thereby removing the need to precompute the ROQ bases.

Finally, likelihood-free methods to accelerate PE mainly consist of ML models pretrained on simulated data to approximate the likelihood or posterior distributions [34–36, 99–104]. Contrary to these pipelines, JIM conducts the PE without the need for pretraining.

C. Environmental impact

Besides a reduction in wall time, our setup additionally offers an ecologically desirable implementation to perform PE.

We compare the carbon footprint of JIM relative to the other pipelines reported in Tab. IV. The TDP of an NVIDIA A100-40 GB GPU, used for the JIM runs, is 400 W [105]. The PBILBY runs used a single Intel Xeon Platinum 8174 Processor with a TDP of 240 W [106]. The RB-BILBY and ROQ-BILBY used a single Intel Xeon Silver 4310 Processor CPU with a TDP of 120 W [81].

| Event | Waveform | JIM | P-BILBY | RB-BILBY | ROQ-BILBY |
|-----------|----------|--------------------|-------------|------------|------------|
| | | (1 GPU) | (480 cores) | (24 cores) | (24 cores) |
| GW170817 | TF2 | (9.70 + 17.00) min | 9.64 h | 3.18 h | — |
| | NRTv2 | (5.69 + 28.02) min | 10.99 h | 4.68 h | 1.65 h |
| GW190425 | TF2 | (5.13 + 16.49) min | 4.08 h | 2.30 h | — |
| | NRTv2 | (6.15 + 15.37) min | 4.69 h | 4.68 h | 0.97 h |
| Injection | TF2 | 24.76 min | — | — | — |
| | NRTv2 | 18.02 min | — | — | — |

TABLE IV: Total wall time spent on conducting PE on the events mentioned in this work, with the `TaylorF2` (TF2) and `IMRPhenomD_NRTidalv2` (NRTv2) waveform models and using the resources mentioned in the main text for benchmarking. For the real events analyzed with JIM, we quote the time spent on EVOSAX and FLOWMC separately. For the injections, we quote the median wall time. These wall times depend highly on the hardware used for conducting the analysis, i.e., one can achieve a shorter (longer) wall time if more (fewer) CPUs or GPUs are used.

Based on our PE runs, we take the average wall time for each pipeline, and the TDP reported above to estimate the required energy to produce the results for all 200 injection runs and the 4 real event runs shown in this work. The results are reported in amounts of kWh in Tab. V.⁷ In order to make a fair comparison against JIM, we also report the time taken up by the pretraining phase of the ROQ method, i.e., the time taken to construct the ROQ bases. The details of this estimate can be found in Appendix C. For comparison, the average annual electricity consumption of a Netherlands household in 2021 was 2810 kWh [107].

To translate these into tangible numbers, we will assume that 0.328 kg CO₂ is produced per kWh [108] and that it approximately takes 50 trees a year to capture 1000 kg of CO₂ [109]. Given a year, it takes around 0.55 trees to absorb the amount of CO₂ generated by JIM. On the other hand, around 59.02 and 1.49 trees are needed for absorbing the CO₂ generated by PBILBY and RB-BILBY, respectively. While only 0.52 trees are needed to counter the carbon footprint from the sampling of ROQ-BILBY, the precompute of the ROQ bases requires around 0.44 trees. We can, therefore, conclude that JIM is more environmentally friendly than the other pipelines considered in performing the PE runs in this work. However, we would like to emphasize that the cost associated with building the ROQ bases is a one-time cost only. Therefore, we estimate that ROQ-BILBY will have a similar ecological footprint as JIM after around 3000 PE runs.

| | kWh | CO ₂ [kg] | Trees [†] |
|-----------|-------------------------|----------------------|--------------------|
| JIM | 34 | 11 | 0.55 |
| P-BILBY | 3599 | 1180 | 59.02 |
| RB-BILBY | 91 | 30 | 1.49 |
| ROQ-BILBY | sampling | 32 | 0.52 |
| | precompute [‡] | 27 | 0.44 |

TABLE V: Estimate of the environmental impact of performing all runs in this work with different pipelines. [†]Number of trees needed to capture the emitted CO₂ in a year. [‡]Based on our estimate of the resources needed to build the required ROQ bases, see Appendix C.

D. Future work

Finally, we mention a few directions in which we wish to pursue the developmental work of our pipeline.

While our current approach, as outlined in Sec.II C, allows us to use `IMRPhenomD_NRTidalv2` with the existing relative binning implementation, it is desirable to extend the relative binning method to waveforms which include a tapering window, such as the `NRTidal` family of waveforms. For this, one requires a scheme to construct the bins without making prior assumptions regarding the waveforms used. An example of such an agnostic approach is given by Ref. [110].

In addition, a current bottleneck in the development of JIM is the need for a JAX-compatible implementation of existing GW approximants. At the time of writing, a RIPPLE implementation of the precessing waveforms `IMRPhenomPv2` and `IMRPhenomXPHM` are under development. Additionally, we will investigate the possibility of training surrogate ML models to approximate the waveforms, which removes the need to re-implement waveforms from scratch and reduces development time.

⁷The obtained numbers have been rounded for clarity and ease of presentation.

Furthermore, future work can investigate the integration with existing packages. While our current pipeline produces posterior samples of any desired target distribution, it does not output the evidence, which is crucial for model selection. In the future, we wish to estimate the Bayesian evidence by performing importance sampling on our produced samples. Future work can integrate JIM with DENMARF [111] or HARMONIC [112–114] to obtain the Bayesian evidence. Secondly, one can attempt to integrate the recently introduced package ASTREOS [115] with our pipeline. ASTREOS can generate confidence intervals for the equations of state in less than one second by relying on normalizing flows. However, the NF maps the component masses and tidal deformabilities to a set of so-called auxiliary parameters from which the EOS constraints can be inferred. Obtaining estimates for these intrinsic parameters can be done reliably and efficiently with JIM, which can therefore empower ASTREOS.

VI. CONCLUSIONS

In this work, we have demonstrated the robustness, accuracy, and speed of JIM in performing parameter estimation for gravitational waves of binary neutron star mergers with tidal effects. By combining relative binning, JAX, gradient-based MCMC and normalizing flows, JIM can produce posteriors accurately in the order of minutes without requiring any precomputed input such as a pre-trained normalizing flow. Specifically, we are able to analyze GW170817 and GW190425 with the TaylorF2 and IMRPhenomD_NRTidalv2 waveforms in 21 to 33 minutes of total wall time, depending on the sampling settings and the number of bins used in relative binning. Evaluated on a large suite of simulated events, the median total wall times are below 30 minutes for both waveforms. As such, JIM can be an indispensable tool for future science cases, such as low-latency follow-up strategies and data analysis with next-generation gravitational wave detectors. Additionally, we have shown that JIM has significantly reduced the environmental impact of parameter estimation as compared to other pipelines. Therefore, JIM presents an ecologically sustainable approach to addressing these computationally intensive tasks.

Appendix A: Data availability

All code used to produce the figures in this paper is available at the following link: <https://github.com/ThibeauWouters/TurboPE-BNS>. Posterior samples will be shared upon request.

Appendix B: Corner plots

We show the corner plots of the posterior distributions obtained from JIM and PBILBY in Figures 4 to 7

for the GW170817 and GW190425 events analyzed with TaylorF2 and IMRPhenomD_NRTidalv2. Instead of the individual aligned spins, we plot the χ_{eff} parameter as defined by Eq. (7). Moreover, we show the tidal deformabilities in terms of $\tilde{\Lambda}$ and $\delta\tilde{\Lambda}$, defined by

$$\begin{aligned}\tilde{\Lambda} &= \frac{16}{13} \frac{(m_1 + 12m_2)m_1^4\Lambda_1 + (m_2 + 12m_1)m_2^4\Lambda_2}{(m_1 + m_2)^5}, \\ \delta\tilde{\Lambda} &= \left(\frac{1690}{1319}\eta - \frac{4843}{1319} \right) \frac{m_1^4\Lambda_1 - m_2^4\Lambda_2}{(m_1 + m_2)^4} \\ &\quad + \frac{6162}{1319} \sqrt{1 - 4\eta} \frac{m_1^4\Lambda_1 + m_2^4\Lambda_2}{(m_1 + m_2)^4},\end{aligned}\tag{B1}$$

where $\eta = m_1m_2/(m_1 + m_2)^2$ is the symmetric mass ratio. The plotted contours show the 1σ and 2σ significance levels. Across the four sets of posterior samples shown, we observe qualitative agreement between the ones obtained from JIM and those obtained from PBILBY.

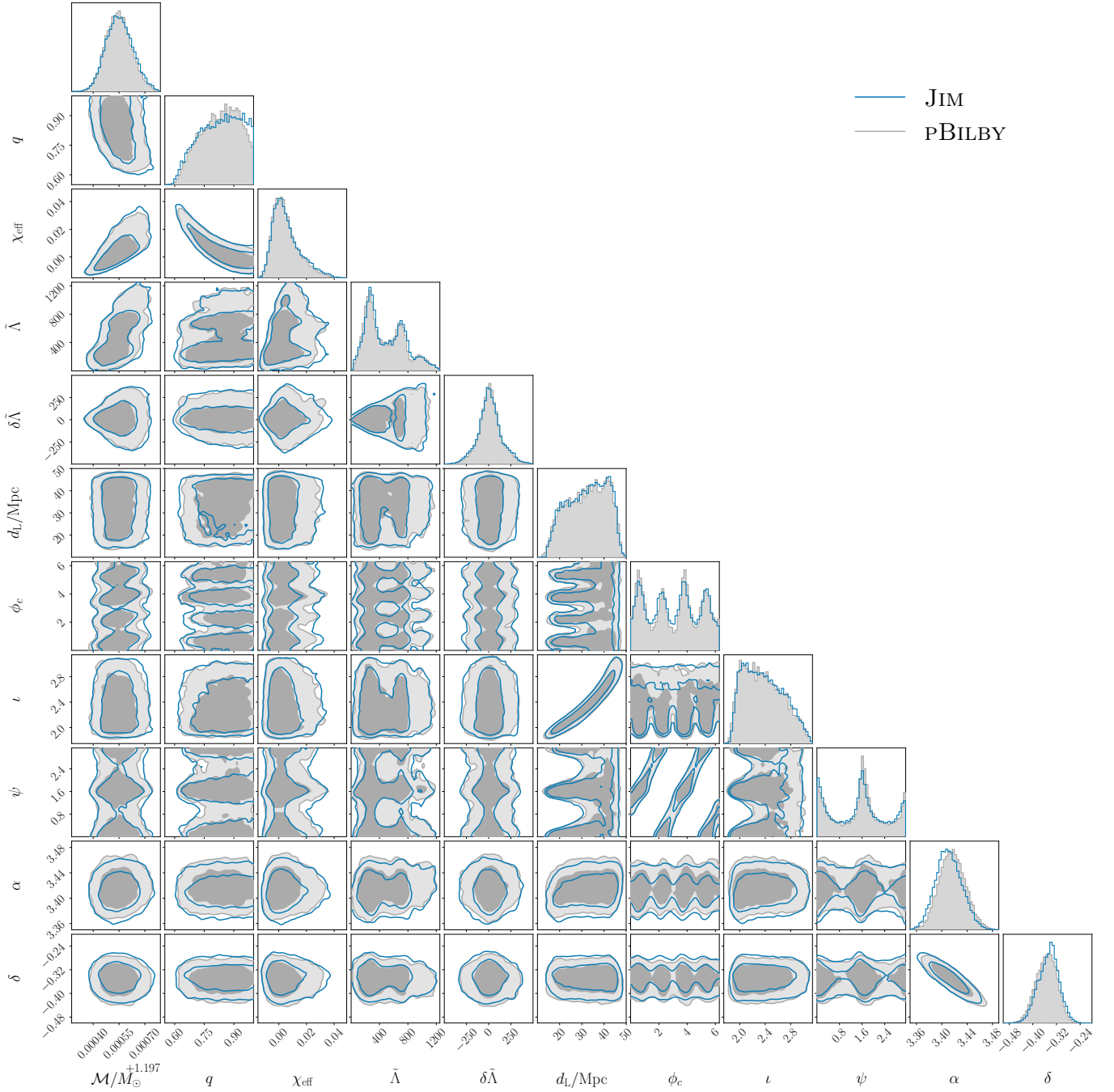


FIG. 4: Comparison of the posterior distributions of GW170817, obtained with the TaylorF2 waveform, using JIM and PBILBY.

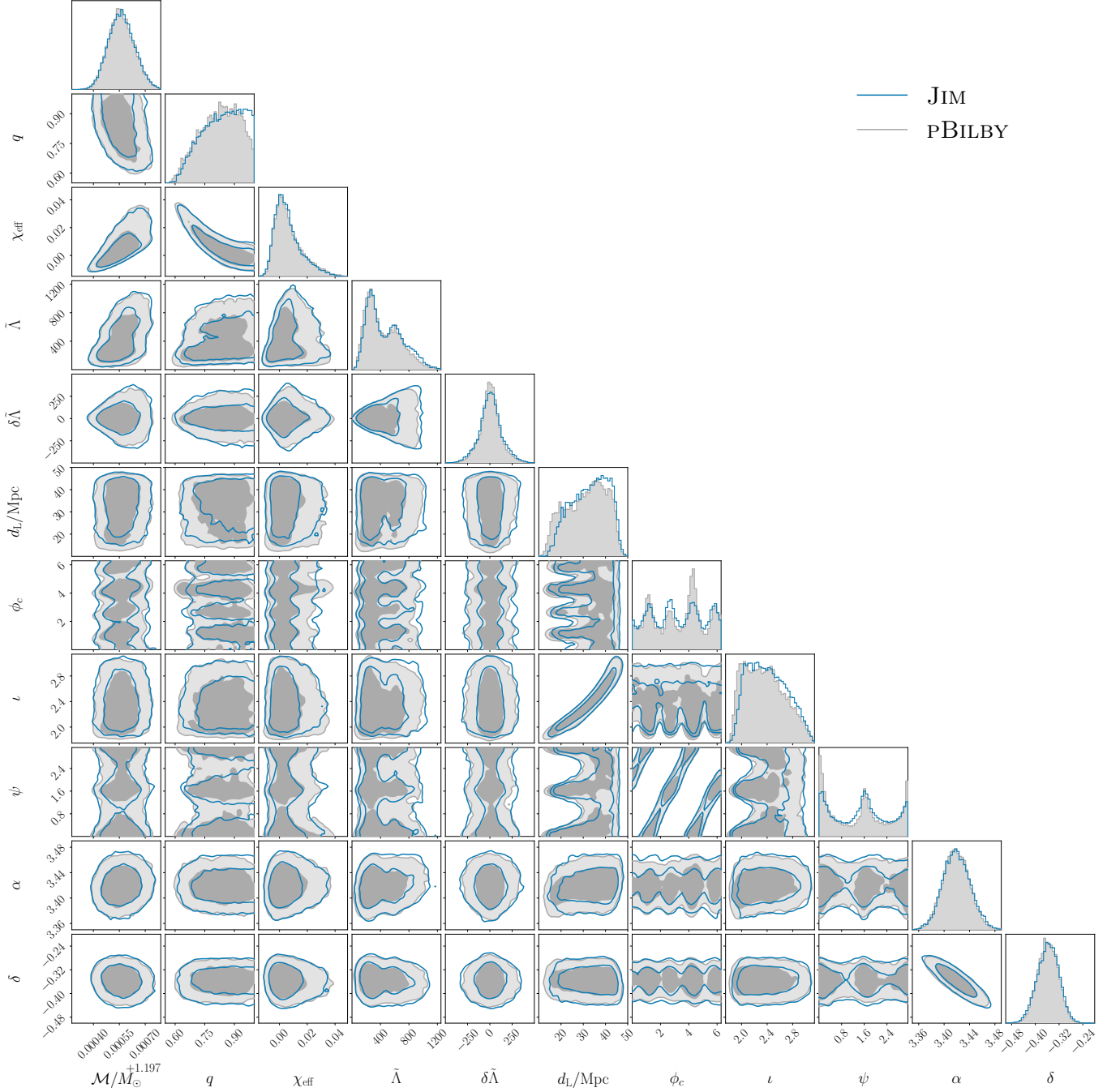


FIG. 5: Comparison of the posterior distributions of GW170817, obtained with the `IMRPhenomD_NRTidalv2` waveform, using `JIM` and `PBILBY`.

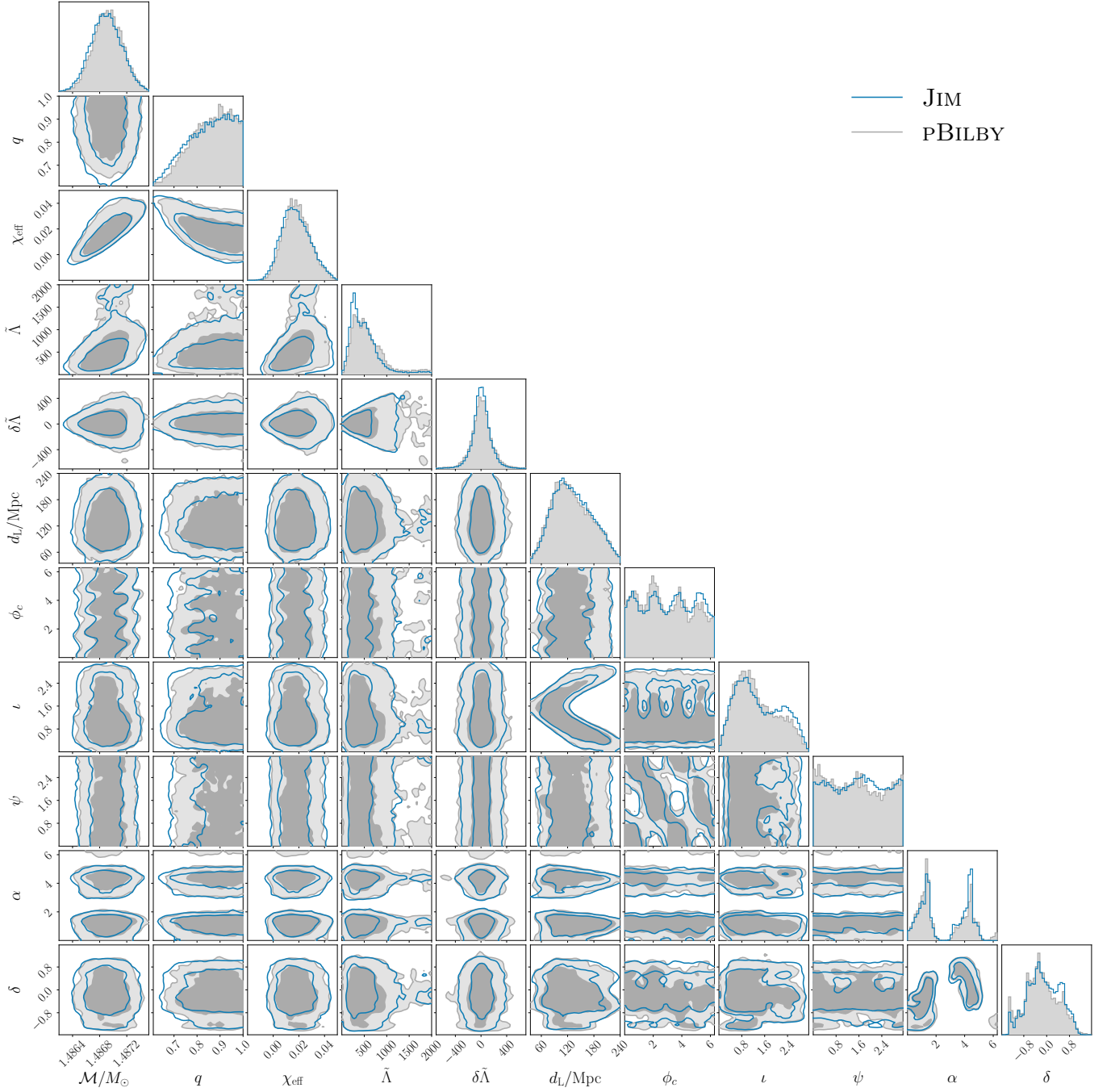


FIG. 6: Comparison of the posterior distributions of GW190425, obtained with the TaylorF2 waveform, using JIM and PBILBY.

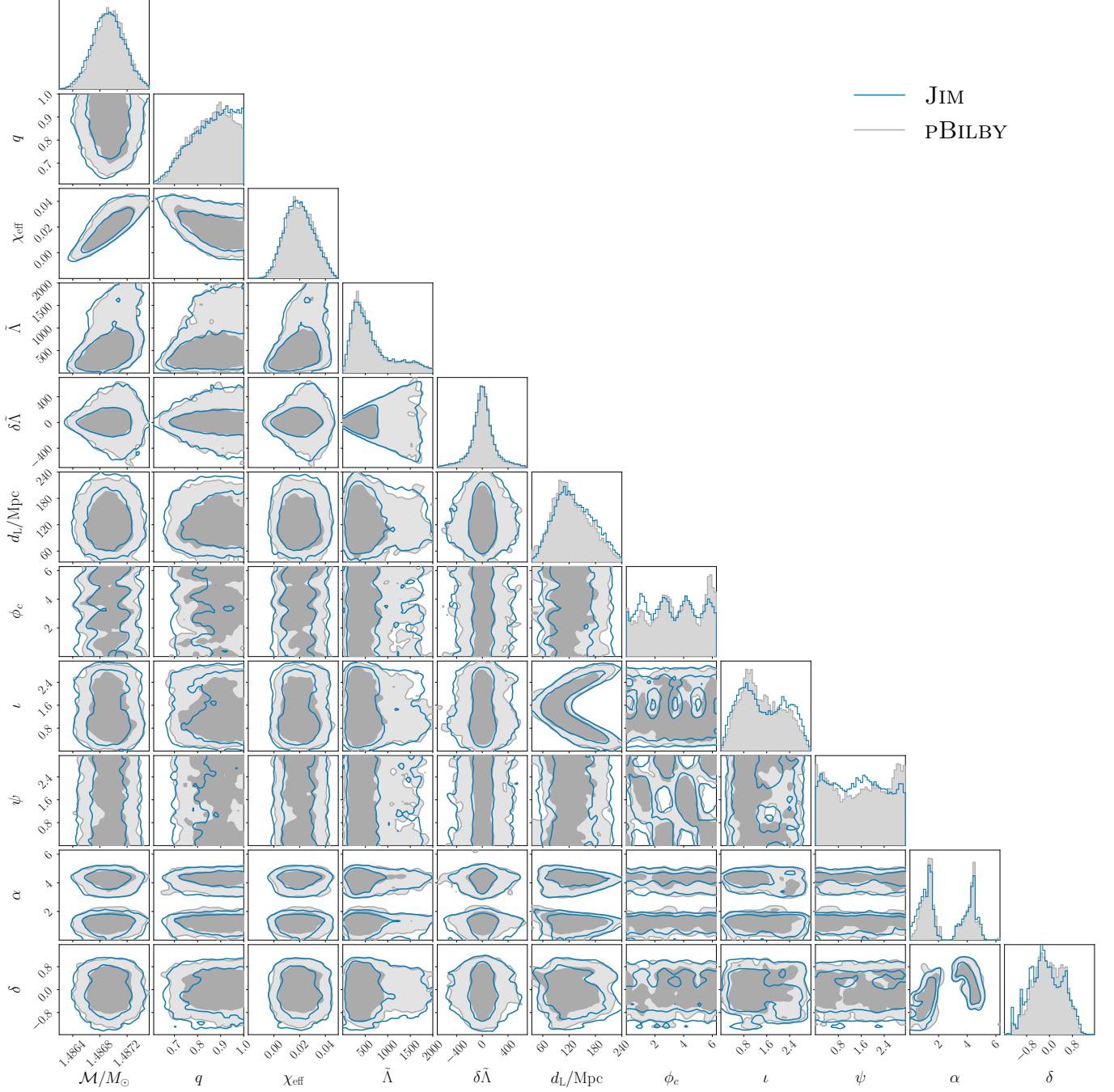


FIG. 7: Comparison of the posterior distributions of GW190425, obtained with the `IMRPhenomD_NRTidalv2` waveform, using JIM and PBILBY.

Appendix C: Estimate of ROQ environmental impact

We provide details on how the estimate of the environmental impact of constructing ROQ bases, reported in Tab. V, is computed based on Ref. [116].

Building the ROQ bases for the `IMRPhenomPv2_NRTidalv2` waveform takes around ~ 1 day when using ~ 100 cores on the NEMO cluster owned by UWM when making use of multi-banding [117] to speed up the building of the ROQ bases. We will assume around ~ 5 Intel Xeon Gold 6136 Processor CPUs were used, each having a TDP of 150 W [118]. Therefore, we estimate the energy consumption of building the ROQ bases for this waveform to be around 27 kWh.

Currently, there is no ROQ implementation of the `TaylorF2` waveform with tidal effects publicly available. To estimate the computational cost to build the ROQ bases for this waveform, we will conservatively assume that this requires around half of the resources used for the `IMRPhenomPv2_NRTidalv2` as the computational cost depends on the complexity of the waveform model.

We would like to emphasize that this is only an estimate of the computational cost. In particular, further advancements in the techniques used for building ROQ bases can potentially reduce the computational cost, e.g. Ref. [119].

ACKNOWLEDGMENTS

We thank Justin Janquart, Harsh Narola, Anna Puecher, Kaze Wong, Thomas Edwards, Nihar Gupte, Michael Williams, Colm Talbot, Lalit Pathak and Soichiro Morisaki for fruitful discussions and feedback that led to the improvement of this work. T.W., P.T.H.P., and C.V.D.B. are supported by the research program of the Netherlands Organization for Scientific Research (NWO). T.W., P.T.H.P., T.D. acknowledge support from the Daimler and Benz Foundation for the

project “NUMANJI”. T.D. acknowledges support from the European Union (ERC, SMArt, 101076369). Views and opinions expressed are those of the authors only and do not necessarily reflect those of the European Union or the European Research Council. Neither the European Union nor the granting authority can be held responsible for them. We thank SURF (www.surf.nl) for the support in using the National Supercomputer Snellius under project number EINF-6587 and EINF-8596. Computations have been performed on the SuperMUC-NG (LRZ) under project number pn56zo. The authors acknowledge the computational resources provided by the LIGO Laboratory’s CIT cluster, which is supported by National Science Foundation Grants PHY-0757058 and PHY0823459. This research has made use of data or software obtained from the Gravitational Wave Open Science Center (gwosc.org), a service of the LIGO Scientific Collaboration, the Virgo Collaboration, and KAGRA. This material is based upon work supported by NSF’s LIGO Laboratory which is a major facility fully funded by the National Science Foundation, as well as the Science and Technology Facilities Council (STFC) of the United Kingdom, the Max-Planck-Society (MPS), and the State of Niedersachsen/Germany for support of the construction of Advanced LIGO and construction and operation of the GEO600 detector. Additional support for Advanced LIGO was provided by the Australian Research Council. Virgo is funded, through the European Gravitational Observatory (EGO), by the French Centre National de Recherche Scientifique (CNRS), the Italian Istituto Nazionale di Fisica Nucleare (INFN) and the Dutch Nikhef, with contributions by institutions from Belgium, Germany, Greece, Hungary, Ireland, Japan, Monaco, Poland, Portugal, Spain. KAGRA is supported by Ministry of Education, Culture, Sports, Science and Technology (MEXT), Japan Society for the Promotion of Science (JSPS) in Japan; National Research Foundation (NRF) and Ministry of Science and ICT (MSIT) in Korea; Academia Sinica (AS) and National Science and Technology Council (NSTC) in Taiwan.

-
- [1] K. W. K. Wong, M. Isi, and T. D. P. Edwards, *Astrophys. J.* **958**, 129 (2023), arXiv:2302.05333 [[astro-ph.IM](#)].
 - [2] J. M. Lattimer, *Ann. Rev. Nucl. Part. Sci.* **62**, 485 (2012), arXiv:1305.3510 [[nucl-th](#)].
 - [3] F. Özel and P. Freire, *Ann. Rev. Astron. Astrophys.* **54**, 401 (2016), arXiv:1603.02698 [[astro-ph.HE](#)].
 - [4] I. Tews *et al.*, *Few Body Syst.* **63**, 67 (2022), arXiv:2202.01105 [[nucl-th](#)].
 - [5] T. Hinderer, B. D. Lackey, R. N. Lang, and J. S. Read, *Phys. Rev. D* **81**, 123016 (2010), arXiv:0911.3535 [[astro-ph.HE](#)].
 - [6] T. Damour and A. Nagar, *Phys. Rev. D* **80**, 084035 (2009), arXiv:0906.0096 [[gr-qc](#)].
 - [7] L. Lindblom, *Astrophys. J.* **398**, 569 (1992).
 - [8] E. E. Flanagan and T. Hinderer, *Phys. Rev. D* **77**, 021502 (2008), arXiv:0709.1915 [[astro-ph](#)].
 - [9] W. Del Pozzo, T. G. F. Li, M. Agathos, C. Van Den Broeck, and S. Vitale, *Phys. Rev. Lett.* **111**, 071101 (2013), arXiv:1307.8338 [[gr-qc](#)].
 - [10] M. Agathos, J. Meidam, W. Del Pozzo, T. G. F. Li, M. Tompitak, J. Veitch, S. Vitale, and C. Van Den Broeck, *Phys. Rev. D* **92**, 023012 (2015), arXiv:1503.05405 [[gr-qc](#)].
 - [11] P. Demorest, T. Pennucci, S. Ransom, M. Roberts, and J. Hessels, *Nature* **467**, 1081 (2010), arXiv:1010.5788 [[astro-ph.HE](#)].

- [12] J. Antoniadis, P. C. Freire, N. Wex, T. M. Tauris, R. S. Lynch, *et al.*, *Science* **340**, 6131 (2013), arXiv:1304.6875 [astro-ph.HE].
- [13] Z. Arzoumanian *et al.* (NANOGrav), *Astrophys. J. Suppl.* **235**, 37 (2018), arXiv:1801.01837 [astro-ph.HE].
- [14] H. T. Cromartie *et al.*, *Nature Astron.* **4**, 72 (2019), arXiv:1904.06759 [astro-ph.HE].
- [15] M. C. Miller *et al.*, *Astrophys. J. Lett.* **887**, L24 (2019), arXiv:1912.05705 [astro-ph.HE].
- [16] T. E. Riley *et al.*, *Astrophys. J. Lett.* **887**, L21 (2019), arXiv:1912.05702 [astro-ph.HE].
- [17] M. C. Miller *et al.*, *Astrophys. J. Lett.* **918**, L28 (2021), arXiv:2105.06979 [astro-ph.HE].
- [18] T. E. Riley *et al.*, *Astrophys. J. Lett.* **918**, L27 (2021), arXiv:2105.06980 [astro-ph.HE].
- [19] B. P. Abbott *et al.* (LIGO Scientific, Virgo), *Phys. Rev. Lett.* **119**, 161101 (2017), arXiv:1710.05832 [gr-qc].
- [20] J. Aasi *et al.* (LIGO Scientific), *Class. Quant. Grav.* **32**, 074001 (2015), arXiv:1411.4547 [gr-qc].
- [21] F. Acernese *et al.* (VIRGO), *Class. Quant. Grav.* **32**, 024001 (2015), arXiv:1408.3978 [gr-qc].
- [22] J. Veitch *et al.*, *Phys. Rev. D* **91**, 042003 (2015), arXiv:1409.7215 [gr-qc].
- [23] C. M. Biwer, C. D. Capano, S. De, M. Cabero, D. A. Brown, A. H. Nitz, and V. Raymond, *Publ. Astron. Soc. Pac.* **131**, 024503 (2019), arXiv:1807.10312 [astro-ph.IM].
- [24] G. Ashton *et al.*, *Astrophys. J. Suppl.* **241**, 27 (2019), arXiv:1811.02042 [astro-ph.IM].
- [25] I. M. Romero-Shaw *et al.*, *Mon. Not. Roy. Astron. Soc.* **499**, 3295 (2020), arXiv:2006.00714 [astro-ph.IM].
- [26] R. J. E. Smith, G. Ashton, A. Vajpeyi, and C. Talbot, *Mon. Not. Roy. Astron. Soc.* **498**, 4492 (2020), arXiv:1909.11873 [gr-qc].
- [27] B. P. Abbott *et al.* (LIGO Scientific, Virgo), *Astrophys. J. Lett.* **892**, L3 (2020), arXiv:2001.01761 [astro-ph.HE].
- [28] N. J. Cornish, (2010), arXiv:1007.4820 [gr-qc].
- [29] B. Zackay, L. Dai, and T. Venumadhav, (2018), arXiv:1806.08792 [astro-ph.IM].
- [30] P. Canizares, S. E. Field, J. R. Gair, and M. Tiglio, *Phys. Rev. D* **87**, 124005 (2013), arXiv:1304.0462 [gr-qc].
- [31] P. Canizares, S. E. Field, J. Gair, V. Raymond, R. Smith, and M. Tiglio, *Phys. Rev. Lett.* **114**, 071104 (2015), arXiv:1404.6284 [gr-qc].
- [32] K. Krishna, A. Vijaykumar, A. Ganguly, C. Talbot, S. Biscoveanu, R. N. George, N. Williams, and A. Zimmerman, (2023), arXiv:2312.06009 [gr-qc].
- [33] S. Morisaki, R. Smith, L. Tsukada, S. Sachdev, S. Stevenson, C. Talbot, and A. Zimmerman, *Phys. Rev. D* **108**, 123040 (2023), arXiv:2307.13380 [gr-qc].
- [34] M. Dax, S. R. Green, J. Gair, J. H. Macke, A. Buonanno, and B. Schölkopf, *Phys. Rev. Lett.* **127**, 241103 (2021), dINGO paper, arXiv:2106.12594 [gr-qc].
- [35] M. Dax, S. R. Green, J. Gair, M. Pürrer, J. Wildberger, J. H. Macke, A. Buonanno, and B. Schölkopf, *Phys. Rev. Lett.* **130**, 171403 (2023), arXiv:2210.05686 [gr-qc].
- [36] U. Bhardwaj, J. Alvey, B. K. Miller, S. Nissanke, and C. Weniger, *Phys. Rev. D* **108**, 042004 (2023), arXiv:2304.02035 [gr-qc].
- [37] M. J. Williams, J. Veitch, and C. Messenger, *Phys. Rev. D* **103**, 103006 (2021), arXiv:2102.11056 [gr-qc].
- [38] M. J. Williams, J. Veitch, and C. Messenger, *Mach. Learn. Sci. Tech.* **4**, 035011 (2023), arXiv:2302.08526 [astro-ph.IM].
- [39] P. T. H. Pang *et al.*, *Nature Commun.* **14**, 8352 (2023), arXiv:2205.08513 [astro-ph.HE].
- [40] J. Veitch and A. Vecchio, *Phys. Rev. D* **81**, 062003 (2010), arXiv:0911.3820 [astro-ph.CO].
- [41] A. Buonanno, B. Iyer, E. Ochsner, Y. Pan, and B. S. Sathyaprakash, *Phys. Rev. D* **80**, 084043 (2009), arXiv:0907.0700 [gr-qc].
- [42] L. Blanchet, *Living Rev. Rel.* **17**, 2 (2014), arXiv:1310.1528 [gr-qc].
- [43] A. Buonanno and T. Damour, *Phys. Rev. D* **59**, 084006 (1999), arXiv:gr-qc/9811091.
- [44] A. Buonanno and T. Damour, *Phys. Rev. D* **62**, 064015 (2000), arXiv:gr-qc/0001013.
- [45] T. Damour and A. Nagar, *Fundam. Theor. Phys.* **162**, 211 (2011), arXiv:0906.1769 [gr-qc].
- [46] S. Bernuzzi, A. Nagar, T. Dietrich, and T. Damour, *Phys. Rev. Lett.* **114**, 161103 (2015), arXiv:1412.4553 [gr-qc].
- [47] A. Nagar *et al.*, *Phys. Rev. D* **98**, 104052 (2018), arXiv:1806.01772 [gr-qc].
- [48] S. Akcay, S. Bernuzzi, F. Messina, A. Nagar, N. Ortiz, and P. Rettegno, *Phys. Rev. D* **99**, 044051 (2019), arXiv:1812.02744 [gr-qc].
- [49] T. Hinderer *et al.*, *Phys. Rev. Lett.* **116**, 181101 (2016), arXiv:1602.00599 [gr-qc].
- [50] J. Steinhoff, T. Hinderer, A. Buonanno, and A. Taracchini, *Phys. Rev. D* **94**, 104028 (2016), arXiv:1608.01907 [gr-qc].
- [51] S. Husa, S. Khan, M. Hannam, M. Pürrer, F. Ohme, X. Jiménez Forteza, and A. Bohé, *Phys. Rev. D* **93**, 044006 (2016), arXiv:1508.07250 [gr-qc].
- [52] S. Khan, S. Husa, M. Hannam, F. Ohme, M. Pürrer, X. Jiménez Forteza, and A. Bohé, *Phys. Rev. D* **93**, 044007 (2016), arXiv:1508.07253 [gr-qc].
- [53] V. Varma, S. E. Field, M. A. Scheel, J. Blackman, D. Gerosa, L. C. Stein, L. E. Kidder, and H. P. Pfeiffer, *Phys. Rev. Research.* **1**, 033015 (2019), arXiv:1905.09300 [gr-qc].
- [54] T. Dietrich, S. Bernuzzi, and W. Tichy, *Phys. Rev. D* **96**, 121501 (2017), arXiv:1706.02969 [gr-qc].
- [55] T. Dietrich, A. Samajdar, S. Khan, N. K. Johnson-McDaniel, R. Dudi, and W. Tichy, *Phys. Rev. D* **100**, 044003 (2019), arXiv:1905.06011 [gr-qc].
- [56] M. Colleoni, F. A. R. Vidal, N. K. Johnson-McDaniel, T. Dietrich, M. Haney, and G. Pratten, (2023), arXiv:2311.15978 [gr-qc].
- [57] A. Abac, T. Dietrich, A. Buonanno, J. Steinhoff, and M. Ujevic, *Phys. Rev. D* **109**, 024062 (2024), arXiv:2311.07456 [gr-qc].
- [58] N. J. Cornish, *Phys. Rev. D* **104**, 104054 (2021), arXiv:2109.02728 [gr-qc].
- [59] N. Hansen and A. Ostermeier, *Evolutionary Computation* **9**, 159 (2001).
- [60] R. T. Lange, “evosax: Jax-based evolution strategies,” (2022), arXiv:2212.04180 [cs.NE].
- [61] R. Frostig, M. J. Johnson, and C. Leary, *Systems for Machine Learning* **4** (2018).
- [62] T. D. P. Edwards, K. W. K. Wong, K. K. H. Lam, A. Coogan, D. Foreman-Mackey, M. Isi, and A. Zimmerman, (2023), arXiv:2302.05329 [astro-ph.IM].

- [63] F. Iacovelli, M. Mancarella, S. Foffa, and M. Maggiore, *Astrophys. J. Supp.* **263**, 2 (2022), arXiv:2207.06910 [astro-ph.IM].
- [64] H. S. Chia, T. D. P. Edwards, D. Wadekar, A. Zimmerman, S. Olsen, J. Roulet, T. Venumadhav, B. Zackay, and M. Zaldarriaga, (2023), arXiv:2306.00050 [gr-qc].
- [65] K. W. k. Wong, M. Gabré, and D. Foreman-Mackey, *J. Open Source Softw.* **8**, 5021 (2023), arXiv:2211.06397 [astro-ph.IM].
- [66] M. Gabré, G. M. Rotskoff, and E. Vanden-Eijnden, *Proc. Nat. Acad. Sci.* **119**, e2109420119 (2022), arXiv:2105.12603 [physics.data-an].
- [67] U. Grenander and M. I. Miller, *Journal of the Royal Statistical Society: Series B (Methodological)* **56**, 549 (1994).
- [68] P. Kidger and C. Garcia, “Equinox: neural networks in jax via callable pytrees and filtered transformations,” (2021), arXiv:2111.00254 [cs.LG].
- [69] LIGO Scientific Collaboration, Virgo Collaboration, and KAGRA Collaboration, “LVK Algorithm Library - LALSuite,” Free software (GPL) (2018).
- [70] M. Pürrer and C.-J. Haster, *Phys. Rev. Res.* **2**, 023151 (2020), arXiv:1912.10055 [gr-qc].
- [71] S. R. Cook, A. Gelman, and D. B. Rubin, *Journal of Computational and Graphical Statistics* **15**, 675 (2006).
- [72] R. J. Foley, D. A. Coulter, C. D. Kilpatrick, A. L. Piro, E. Ramirez-Ruiz, and J. Schwab, *Mon. Not. Roy. Astron. Soc.* **494**, 190 (2020), arXiv:2002.00956 [astro-ph.HE].
- [73] M.-Z. Han, S.-P. Tang, Y.-M. Hu, Y.-J. Li, J.-L. Jiang, Z.-P. Jin, Y.-Z. Fan, and D.-M. Wei, *Astrophys. J. Lett.* **891**, L5 (2020), arXiv:2001.07882 [astro-ph.HE].
- [74] K. Kyutoku, S. Fujibayashi, K. Hayashi, K. Kawaguchi, K. Kiuchi, M. Shibata, and M. Tanaka, *Astrophys. J. Lett.* **890**, L4 (2020), arXiv:2001.04474 [astro-ph.HE].
- [75] T. Hinderer *et al.*, *Phys. Rev. D* **100**, 06321 (2019), arXiv:1808.03836 [astro-ph.HE].
- [76] M. W. Coughlin and T. Dietrich, *Phys. Rev. D* **100**, 043011 (2019), arXiv:1901.06052 [astro-ph.HE].
- [77] R. Abbott *et al.* (LIGO Scientific, Virgo), *SoftwareX* **13**, 100658 (2021), arXiv:1912.11716 [gr-qc].
- [78] R. Abbott *et al.* (KAGRA, VIRGO, LIGO Scientific), *Astrophys. J. Suppl.* **267**, 29 (2023), arXiv:2302.03676 [gr-qc].
- [79] J. Lin, *IEEE Transactions on Information Theory* **37**, 145 (1991), URL: <http://ieeexplore.ieee.org/xpl/articleDetails.jsp?arnumber=61115>.
- [80] J. Skilling, *Bayesian Analysis* **1**, 833 (2006).
- [81] Intel Corporation, “Intel Xeon Silver 4310 Processor,” URL: <https://www.intel.com/content/www/us/en/products/sku/215277/intel-xeon-silver-4310-processor-18m-cache-2-10-ghz/specifications.html>. Accessed: 2024-04-11.
- [82] L. P. Singer and L. R. Price, *Phys. Rev. D* **93**, 024013 (2016), arXiv:1508.03634 [gr-qc].
- [83] C. Stachie *et al.*, *Mon. Not. Roy. Astron. Soc.* **505**, 4235 (2021), arXiv:2103.01733 [astro-ph.HE].
- [84] M. Punturo *et al.*, *Class. Quant. Grav.* **27**, 084007 (2010).
- [85] M. Maggiore *et al.*, *JCAP* **03**, 050 (2020), arXiv:1912.02622 [astro-ph.CO].
- [86] M. Evans *et al.*, (2023), arXiv:2306.13745 [astro-ph.IM].
- [87] M. Branchesi *et al.*, *JCAP* **07**, 068 (2023), arXiv:2303.15923 [gr-qc].
- [88] A. Samajdar, J. Janquart, C. Van Den Broeck, and T. Dietrich, *Phys. Rev. D* **104**, 044003 (2021), arXiv:2102.07544 [gr-qc].
- [89] E. Pizzati, S. Sachdev, A. Gupta, and B. Sathyaprakash, *Phys. Rev. D* **105**, 104016 (2022), arXiv:2102.07692 [gr-qc].
- [90] D. Finstad and D. A. Brown, *Astrophys. J. Lett.* **905**, L9 (2020), arXiv:2009.13759 [astro-ph.IM].
- [91] G. Raaijmakers *et al.*, *Astrophys. J.* **922**, 269 (2021), arXiv:2102.11569 [astro-ph.HE].
- [92] S. Morisaki and V. Raymond, *Phys. Rev. D* **102**, 104020 (2020), arXiv:2007.09108 [gr-qc].
- [93] C. Pankow, P. Brady, E. Ochsner, and R. O’Shaughnessy, *Phys. Rev. D* **92**, 023002 (2015), arXiv:1502.04370 [gr-qc].
- [94] J. Lange, R. O’Shaughnessy, and M. Rizzo, (2018), arXiv:1805.10457 [gr-qc].
- [95] D. Wysocki, R. O’Shaughnessy, J. Lange, and Y.-L. L. Fang, *Phys. Rev. D* **99**, 084026 (2019), arXiv:1902.04934 [astro-ph.IM].
- [96] L. Pathak, A. Reza, and A. S. Sengupta, *Phys. Rev. D* **108**, 064055 (2023), arXiv:2210.02706 [gr-qc].
- [97] L. Pathak, S. Munishwar, A. Reza, and A. S. Sengupta, *Phys. Rev. D* **109**, 024053 (2024), arXiv:2309.07012 [gr-qc].
- [98] J. Roulet, J. Mushkin, D. Wadekar, T. Venumadhav, B. Zackay, and M. Zaldarriaga, (2024), arXiv:2404.02435 [gr-qc].
- [99] H. Gabbard, C. Messenger, I. S. Heng, F. Tonolini, and R. Murray-Smith, *Nature Phys.* **18**, 112 (2022), arXiv:1909.06296 [astro-ph.IM].
- [100] A. Kolmus, G. Baltus, J. Janquart, T. van Laarhoven, S. Caudill, and T. Heskes, *Phys. Rev. D* **106**, 023032 (2022), arXiv:2111.00833 [gr-qc].
- [101] A. Kolmus, J. Janquart, T. Baka, T. van Laarhoven, C. Van Den Broeck, and T. Heskes, (2024), arXiv:2403.02443 [astro-ph.IM].
- [102] A. J. K. Chua and M. Vallisneri, *Phys. Rev. Lett.* **124**, 041102 (2020), arXiv:1909.05966 [gr-qc].
- [103] S. R. Green, C. Simpson, and J. Gair, *Phys. Rev. D* **102**, 104057 (2020), arXiv:2002.07656 [astro-ph.IM].
- [104] S. R. Green and J. Gair, *Mach. Learn. Sci. Tech.* **2**, 03LT01 (2021), arXiv:2008.03312 [astro-ph.IM].
- [105] NVIDIA Corporation, “NVIDIA A100 Tensor Core GPU Data Sheet,” (2024), URL: <https://www.nvidia.com/content/dam/en-zz/Solutions/Data-Center/a100/pdf/nvidia-a100-datasheet-nvidia-us-2188504-web.pdf>. Accessed: 2024-03-27.
- [106] Intel Corporation, “Intel Xeon Platinum 8174 Processor,” (2024), URL: <https://ark.intel.com/content/www/us/en/ark/products/136874/intel-xeon-platinum-8174-processor-33m-cache-3-10-ghz.html>. Accessed: 2024-03-27.
- [107] Statistics Netherlands, “Energy consumption private dwellings; type of dwelling and regions,” (2023), <https://www.cbs.nl/en-gb/figures/detail/81528ENG>. Accessed: 2024-04-02.
- [108] CO2 emissiefactoren, “Lijst emissiefactoren,” (2024), URL: <https://www.co2emissiefactoren.nl/lijst-emissiefactoren/>. Accessed: 2024-04-02.
- [109] Anthesis Climate Neutral group, “What exactly is 1 tonne of CO₂?” (2024), URL: <https://www.climateneutralgroup.com/en/news/what-exactly-is-1-tonne-of-co2-v2/>. Accessed: 2024-03-

- 27.
- [110] H. Narola, J. Janquart, Q. Meijer, K. Haris, and C. Van Den Broeck, (2023), arXiv:2308.12140 [gr-qc].
 - [111] R. K. L. Lo, “DENMARF: a Python package for density estimation using masked autoregressive flow,” (2023), arXiv:2305.14379 [astro-ph.IM].
 - [112] J. D. McEwen, C. G. R. Wallis, M. A. Price, and A. S. Mancini, “Machine learning assisted bayesian model comparison: learnt harmonic mean estimator,” (2023), arXiv:2111.12720 [stat.ME].
 - [113] A. Spurio Mancini, M. M. Docherty, M. A. Price, and J. D. McEwen, (2022), 10.1093/rasti/rzad051, arXiv:2207.04037 [astro-ph.CO].
 - [114] A. Polanska, M. A. Price, A. S. Mancini, and J. D. McEwen, “Learned harmonic mean estimation of the marginal likelihood with normalizing flows,” (2024), arXiv:2307.00048 [stat.ME].
 - [115] J. McGinn, A. Mukherjee, J. Irwin, C. Messenger, M. J. Williams, and I. S. Heng, (2024), arXiv:2403.17462 [gr-qc].
 - [116] Soichiro Morisaki, Personal e-mail correspondence (2024), 16 April 2024.
 - [117] S. Morisaki, Phys. Rev. D **104**, 044062 (2021), arXiv:2104.07813 [gr-qc].
 - [118] Intel Corporation, “Intel Xeon Gold 6136 Processor,” (2024), URL: <https://ark.intel.com/content/www/us/en/ark/products/120479/intel-xeon-gold-6136-processor-24-75m-cache-3-00-ghz.html>. Accessed: 2024-04-17.
 - [119] G. Morras, J. F. N. Siles, and J. Garcia-Bellido, Phys. Rev. D **108**, 123025 (2023), arXiv:2307.16610 [gr-qc].